1 **Long-term carbon sequestration in the Eocene of the Levant Basin through transport of**

2 **organic carbon from nearshore to deep marine environments**

3 Aaron Meilijson[a,b,*], Or M. Bialik[a,c], F. Garrett Boudinot[b], Paul R Bown[d], Chaim Benjamini[e],

4 Nicolas D. Waldmann[a], Julio Sepúlveda[b]

5

6   [a]The Dr. Moses Strauss Department of Marine Geosciences, Charney School of Marine

7 Sciences, University of Haifa, Mount Carmel, 31905 Haifa, Israel.

8   [b]Department of Geological Sciences and Institute of Arctic and Alpine Research

9 (INSTAAR), University of Colorado Boulder, Boulder, Colorado 80309, USA.

10   [c]Institute of Geology and Palaeontology, University of Münster, Corrensstrasse 24, 48149

11 Münster, Germany.

12   [d]Department of Earth Sciences, University College London, Gower Street, London WC1E

13 6BT, UK.

14   [e]Department of Geological and Environmental Sciences, P.O. Box 653, Ben Gurion

15 University of the Negev, 84105 Beer Sheva, Israel.

16

17   [*]Correspondence to: Dr. Aaron Meilijson email: ameilijs@campus.haifa.ac.il Tel: +972-

18 505666926

Abstract

This study addresses a specific component associated with mass transport complexes in marine systems: the role of hyperpycnal flows, dense shelf water cascading, submarine canyons, distributary channels, and other transport mechanisms in transferring organic matter from continental and shallow marine settings into deep-marine environments. We speculate that during the Eocene, allowing for only 0.1‰ of shelf carbon to be preserved through transport mechanisms would account for up to 13.7% of all organic carbon burial. As such, the potential to mobilize through this mechanism large quantities of organic carbon is significant.

Our case study focuses on a 150 m Eocene sequence composed of organic-rich chalks interleaved with displaced neritic limestones. TOC values range between 1.5 and 14%, averaging 4.5%. Displaced limestones are composed of a variety of poorly cemented mud- and wackestones, with low-diversity assemblages of large benthic foraminifera associated with planktonic foraminifera, suggesting deposition under low-energy conditions within the oligophotic zone on the outer ramp. Transport overprints include soft-sediment deformation, partially lithified rip-ups, folds, small diapirs, bed-scale imbrication, brecciation and syn-sedimentary shear. These features indicate detachment, movement and emplacement following initial sedimentation, in some cases more than once. Emplacement occurs into a chalk facies that can vary in appearance from darker (higher TOC) and lighter (lower TOC) lithofacies.

Combination between the sedimentological, petrophysical, and elemental analyses indicates shifts between autochthonous and allochthonous sedimentation, whereas the organic geochemical analysis reveals a correlation between modes of sedimentation and preservation/composition of organic matter. Organic richness seems to increase within intervals of allochthonous sedimentation, with lower TOC values within intervals of autochthonous sedimentation. Organic matter preservation is enhanced due to poor

44   oxygenation of the sea floor, further depleted by rapid burial beneath mass-transport deposits,

45   increasing sedimentation rates and thus organic matter preservation. Horizons rich in organic

46   matter may be derived from three different sources: organic matter with a fingerprint of

47   terrestrial sources (e.g., enhanced contribution of plant leaf waxes) transported from

48   nearshore environments; an allochthonous marine fingerprint with sulfurized hopanoids,

49   which seem to be reworked from pre-existing Cretaceous organic-rich carbonates entrained

50   within fined-grained micro-turbidites in the para-autochthonous facies; and productivity-

51   derived organic matter deposited on the seafloor of the deep marine environment.

52   This study demonstrates how transport mechanisms allow for the long-term burial of

53   organic carbon in marine systems. When taking into consideration similar processes reported

54   to occur in the world oceans today, it is clear that sediment transport and long-term burial of

55   organic carbon is a fundamental part of the global carbon cycle.

56

57   **Keywords:** *Sedimentology, geochemistry, carbon cycle, transport deposits, organic matter.*

1. Introduction

Continental slopes are morphological structures connecting the shallow shelf zone with the deep abyssal plains. Slides, mass transport, and associated hyperpycnal flows, typically erode the outer continental shelf and the upper parts of the slope, and through submarine canyons, transport large volumes of sediments and organic matter (OM) to deep water environments (Bauer and Druffel, 1998). Organic matter may accumulate on the seafloor of the lower slope and adjacent deep basins before finally, being sequestered in the rock record if proper conditions for preservation (i.e., low oxygen conditions and rapid burial) exist. In the geological record, such continental margin canyons can feed sedimentary systems consisting of submarine mass transport complexes (MTCs) worldwide (Coleman and Prior, 1988; Embley, 1980; Evans et al., 2005; Frey-Martinez et al., 2005; Shanmugam, 2000; Woodcock, 1979).

This study addresses a specific component associated with MTCs: the role of hyperpycnal flows, dense shelf water cascading (DSWC; Canals et al., 2006), and mass sediment transport via submarine canyons, distributary channels, and other transport mechanisms, in transferring of OM from continental and shallow marine settings into deep-marine environments. The rapid sedimentation nature of the MTC facilitates efficient OM burial. Moreover, hyperpycnal flows may diminish diffusive and advective ion exchange (Bialik et al., 2022), which may diminish microbial degradation rates. The combined effect of these phenomena has a significant impact on the amount of carbon stored in marine sediment systems adjacent to continents. While this component has been addressed in modern systems (Canals et al., 2006), it remains understudied with regards to deep-time depositional systems.

When a large mass of organic carbon is buried within ancient marine systems, the identification and understanding of OM transport dynamics serve as a key for quantifying its role in the carbon cycle at a global scale. In fact, mass-balance calculations suggest that

83 dissolved organic carbon (DOC) and suspended particulate organic carbon (POC_{susp}) inputs

84 from ocean margins (near shore, usually proximally to the shelf break) to the ocean floor may

85 be more than an order of magnitude greater than organic carbon produced near the ocean

86 surface today (Barrõn and Duarte, 2015; Bauer and Druffel, 1998; Chen et al., 2021). The rates

87 of organic matter burial in deep sediment can influence its preservation and degradation, its

88 potential to yield hydrocarbons, and the amount of CO_2 it releases to the surface waters and

89 eventually the atmosphere. An increase in the velocity of this transport mechanism will have a

90 direct influence on the locking conditions for carbon and its sequestration in sediments (Bianchi

91 et al., 2018; Blair and Aller, 2012; Eglinton et al., 2021; Regnier et al., 2022) . Elucidating the

92 mechanisms of sediment and energy transfer of OM from shallow to deep marine settings via

93 submarine canyons, hyperpycnal flows, DSWC, nepheloid layers (Inthorn et al., 2006), and

94 other transport mechanisms, is crucial for our understanding of carbon flux in deep-water

95 ecosystems and its potential role in modulating global climate dynamics (Talling et al., 2023).

96   This study focuses on the transport of sediment and OM to deep marine settings in the Levant

97 Basin during the early Eocene and demonstrates how proximal OM is transported and mixed

98 with in-situ OM production before being sequestered in deeper settings.

99 2. Material and Methods

100   The GHPS-1 core (Figs. 1 and 2) was drilled in the Gilboa Ridge in 2010 as part of a

101 preliminary geotechnical survey for a hydroelectrical project (Electra Pumped Storage Ltd.).

102 A 571 m-long nearly continuous core, retrieved with >90% recovery, provides an exceptionally

103 well-preserved record of sediments from the Lower to Middle Eocene. The core was

104 systematically logged, described, and selectively sampled for physical and geochemical

105 analyses.

106

107
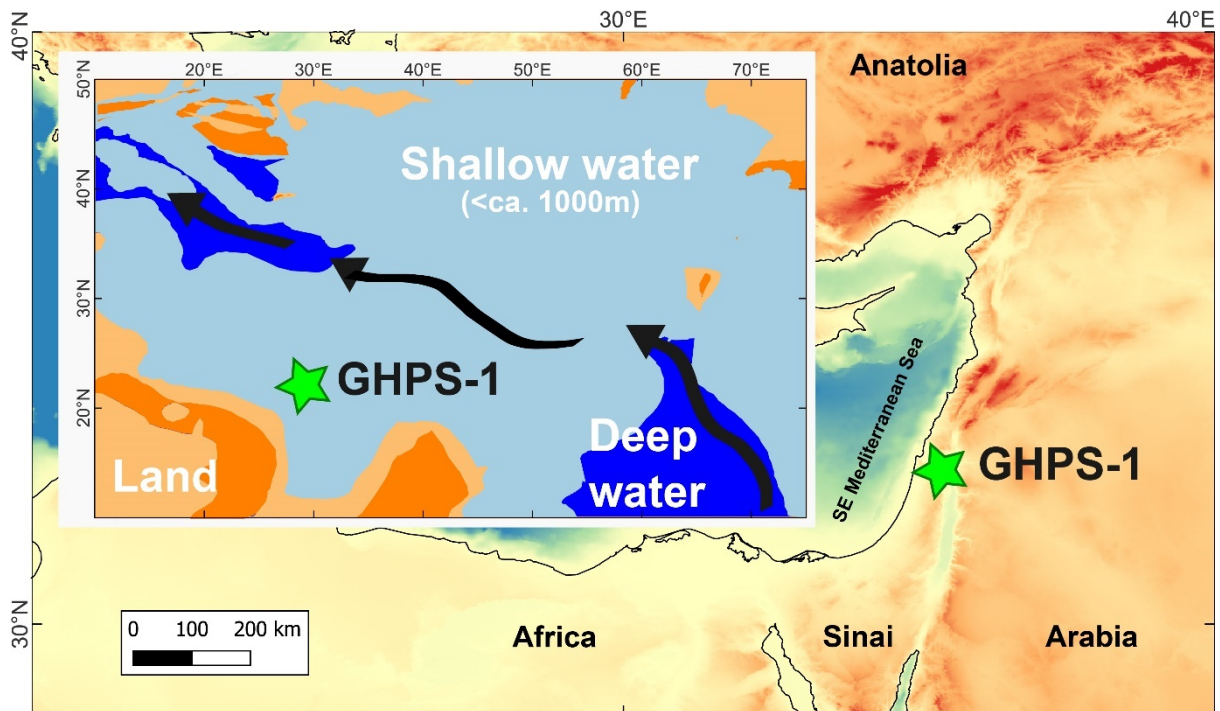
108 *Figure 1. A shaded relief map of the Levant Basin and surrounding area* (Amante and Eakins, 2009) *showing the*

109 *modern position of the GHPS-1core in the Gilboa Ridge in northern Israel. Insert depicts the regional paleogeography of*

110 *the early Eocene (Cao et al., 2017) and the paleo position of the GHPS-1 core. Black arrows in inset indicate the direction*

111 *of the principal surface water flow.*

112 *2.1 Petrophysical analysis*

113   Non-destructive petrophysical analyses were carried out on complete core sections and

114 included measurements of gamma density, magnetic susceptibility, and sonic velocity (P-

115 wave). These parameters were measured using a Geotek Multi Sensor Core Logger (MSCL).

116 *2.2 Petrographic analysis*

117   Thirty thin sections were made from the GHPS-1 core samples for petrographic analysis. The

118 samples were polished with a 1 μm aluminum oxide, glued to a glass slide and polished again

119 to a thickness of 30 μm. The petrographic characteristics and faunal assemblages were

120 documented and photographed. The interpretation of the thin section closely follows

121 procedures outlined in Flügel (2010).

2.3 XRF elemental analysis

We selected 115 samples, representing the full range of lithology and facies as well as temporal distribution across the entire studied interval, for detailed elemental examination. Point sampling was conducted for each interval using a handheld Niton XL3t GOLDD+ XRF analyzer at resolutions of 10 to 1 cm, depending on heterogeneity levels. Measurements were applied to surfaces cleaned with distilled water and air dried, or to powdered material, depending on hardness and reactiveness of the sample. Some 236 spots were analyzed for Ba, Mg, Al, K, Zr, Sr, Zn, Fe, Cr, Ti, Ca, P, Si and S from these samples. Each data point was assigned a lithological character based on core properties and organic content. Data quality was controlled in relation to carbonate content, the value to error ratio, and background level. Mg and K were not included in some analyses because they were present below the limit of detection. Statistical analysis was carried out using the PAST statistical package (Hammer et al., 2001). A correlation matrix was generated for all elements in PAST (Hammer et al., 2001) to calculate the Pearson's correlation coefficient and p-value. Subsequently root arcsin was applied to the data for ordination analysis, PCA analysis was carried out using PAST.

2.4 Organic and inorganic carbon content and pyrolysis data

Total organic and inorganic carbon content (TIC and TOC, respectively) were measured on the same intervals from 253 evenly distributed samples using a Primacs SLC analyzer. For this analysis, ~1-2 g of rock was crushed into fine powder, dried overnight at 50˚C, and cooled in a desiccation chamber prior to further analysis. Additionally, ~20-60 mg of dried powder from 46 of these samples were analyzed by Rock-Eval pyrolysis using a Rock-Eval IV (Vinci Technologies). Rock-Eval measures free hydrocarbons, kerogen-bound hydrocarbons, and the carbon and sulfur content of a rock (Espitalie et al., 1977; Peters, 1986).

145   *2.5 Biomarker analysis*

146   We studied lipid biomarkers in a selected number of intervals to gain insights into variations

147   of OM sources and the degree of thermal alteration. Biomarker extraction, processing and

148   analysis followed the methods described in (Boudinot and Sepúlveda, 2020; Meilijson et al.,

149   2019). Aliphatic hydrocarbons were analyzed on full scan and selective reaction monitoring

150   (SRM) modes via gas chromatography – triple quadrupole-mass spectrometry (GC-QQQ-MS)

151   using a Thermo Trace 1310 Gas Chromatograph interphase to a TSQ Evo 8000 triple

152   quadrupole mass spectrometer (GC-QQQ-MS).

153   **3. Results**

154   *3.1 Age, lithology, and organic richness*

155   The lower 170 m of the GHPS-1 core include an organic-rich carbonate facies (Fig. 2). This

156   sedimentary facies is unique for this period in the Levant region, which is usually characterized

157   by organic-poor white chalks and occasional chert (Supplementary 5). Total organic carbon

158   values ranged between 1.5 and 14 wt.%, averaging 3.5 wt.% (Fig. 2). While reworked material

159   is apparent in the GHPS-1 core, the biostratigraphy of a few samples indicates Early to Middle

160   Eocene ages for the organic-rich sequence, covering the NP13 to MP14 time intervals

161   (Supplementary 7).

162   Several lithofacies were identified in the investigated part of the core (Fig. 2): neritic-rich

163   limestone, chert-rich chalk, organic-poor and organic-rich chalk and marl (which can be either

164   well bedded or highly bioturbated). Chalky sediments containing planktic foraminifera, deep-

165   water benthic foraminifera, radiolarians, and variable amounts of chert (nodules) are typically

166   undisturbed and represent a deep-water depositional setting (Fig. 2C). While organic content

167   is more elevated in darker intervals, organic-lean parts of the core typify the lighter sequences

168   (Fig. 2E, D). The transition from high to low (or undetectable) TOC content occurs at ~400 m

169   depth, concurrent with a shift in the lithology from dark and brown to light white chalk and

170   limestone (Fig. 2C to I versus A and B, respectively).

171   Macroscopic observations coupled with petrographic analysis reveal a plethora of

172   sedimentary indications for lateral transport into a deep basin (Figs. S1-S3). Much of the cored

173   section is composed of limestone units ranging from 5-20 m in thickness, emplaced onto the

174   chalk lithofacies (Fig. 2). The units are variable in thickness and facies composition, tracking

175   a spectrum ranging from algal and nummulitid limestone, rich in rip-ups, to non-bedded,

176   slumped muddy nodular limestones. Subunits tend to truncate previously deposited material

177   along chalky contacts that display shear features. There are also thinner displaced horizons, <1

178   m to a few tens of cm thick, that more visibly interlaminate with autochthonous chalk.

179
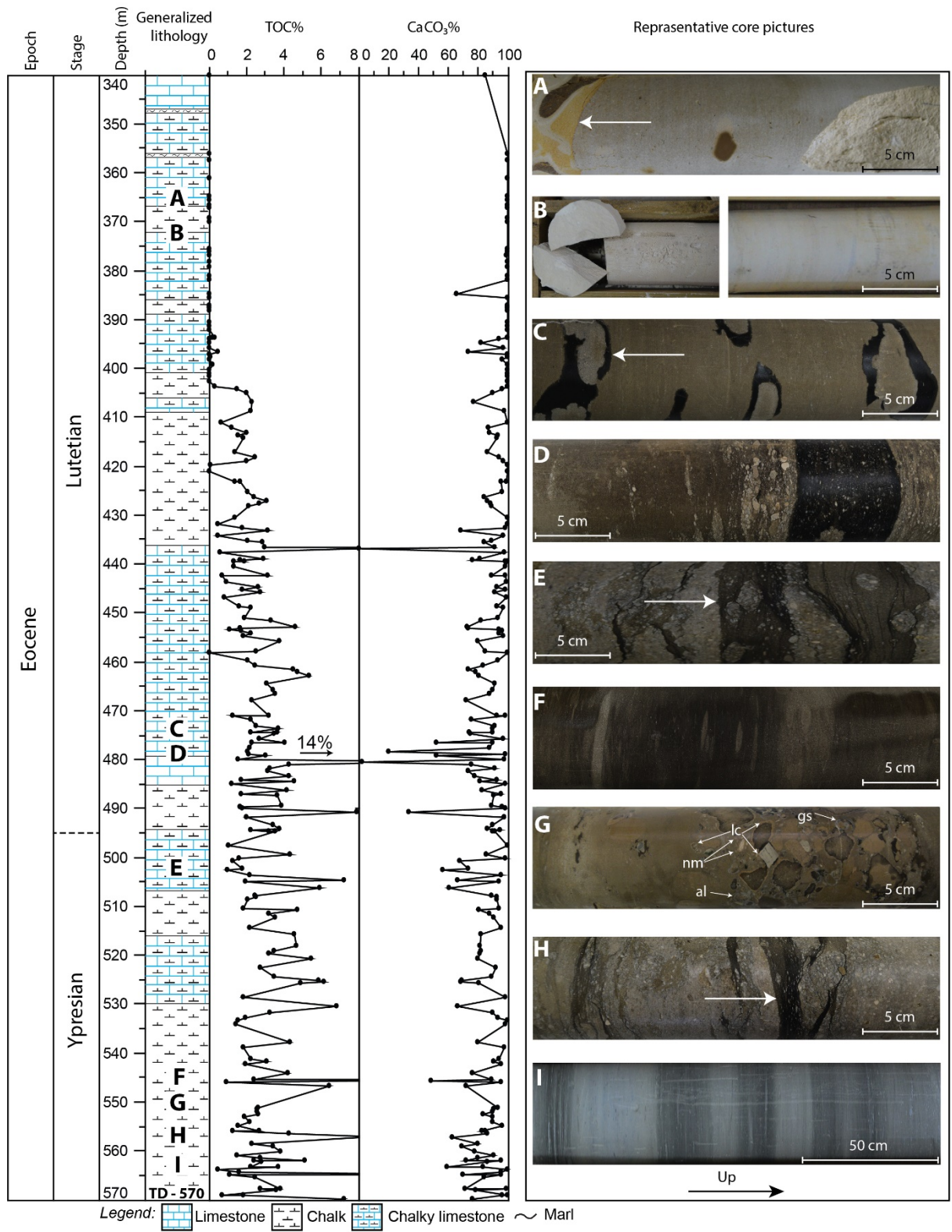
Figure 2. *Left:* Columnar section of the GHPS-1 core in the Gilboa Ridge. Only generalized lithology is shown, in which

the marked lithology is the most common in that interval. Meter-scale variations are common along the core. The top of the

organic rich interval (reaching 14 wt.% and average on 3.5 wt.%) is located at ~400 m. *Right:* Representative photographs

of the GHPS-1 core lithologies, their position is marked on the lithological column on the left. Scale bar is indicated for each

184   *picture, and arrow at bottom right marks the orientation. (A; 366 m) Allochthonous light nummulitic limestone emplaced onto*

185   *autochthonous pelagic chalk with abundant chert lenses. (B; 372 m) Soft white chalk. (C; 474.3 m) Chert-filled borrows within*

186   *organic-rich light brown chalk. (E; 474). (F; 545 m) Rich assemblages of large benthic foraminifera, rhodophycean algae,*

187   *bio- and lithoclasts, emplaced onto brown pelagic chalk. Note the smaller grain size relative to (E) and the ~3 cm silicified*

188   *nummulitic interval within the slump deposits. A transported mass deposit consisting of large, irregular, poorly sorted, at*

189   *times coated grains of a variety of lithoclasts (lc), large gastropods (gs), large calcareous algal fragments (al), and nummulites*

190   *(nm). Grains are part of a slumped body emplaced into autochthonous chalks. (G; 550 m) Alternation between light and darker*

191   *gray chalks. Note the horizontal exaggeration as indicated by the scale bar. (H; 556, D; 525) Black bituminous fine-grained*

192   *veins and laminae filling the pores within the transported nummulitic limestone. (I; 563 m) The darkest bituminous chalks*

193   *along the core appear at its lowest part, corresponding to elevated TOC values.*

194   The transported limestone units are highly variable and are composed of grains, lithoclasts,

195   internally deformed muddy limestone, or large detached clasts. Petrographical examination

196   reveals components such as reworked Cretaceous foraminifera with micritized walls and

197   pressure solution features, large benthic foraminifera (LBF) such as nummulites, pelagic

198   crinoid, and other echinoderm plates, and rhodophycean algae. Furthermore, there are

199   indicators for early diagenesis such as partial early lithification, euhedral dolomite nucleation

200   crystals and incipient dolomitization.

201   *3.2 Petrophysical properties and elemental composition of the GPHS-1 core*

202   Magnetic susceptibility, sonic velocity, and gamma-density show a good correspondence to

203   the lithological variations (Fig. S4). While density increases in the organic-rich carbonate

204   facies, possibly as a result of increased clay particles, sonic velocity decreases. In turn, high

205   magnetic susceptibility values are regularly associated with the emplaced limestone subunits,

206   corresponding to a likely increase in ferromagnetic minerals, taken to reflect augmentation in

207   terrestrial allogenic influx.

208   The two most common elements are Ca (23 to 46 %wt.) and Si (0.6 to 20 %wt.), with high

209   amounts of S (up to 5%wt.) in the darker intervals. Ba, Fe, Zn, P and Si are more abundant

210   below 530 m, although all elements exhibit high levels of variability at a cm-scale resolution.

211 P, Si, Al, Zn and Fe are significantly enriched in the darker (OM-rich) end member facies when

212 compared with the light (organic-poor) end member facies, with mean values of 0.15 ± 0.06,

213 5.1 ± 2.8, 0.87 ± 0.32, 0.014 ± 0.006, 0.68 ± 0.19 %wt. (respectively) (n=39). On the other hand, in

214 the light end member facies, these elements are characterized by mean values of 0.11 ± 0.04,

215 1.7 ± 0.5, 0.38 ± 0.12, 0.008 ± 0.007, and 0.16 ± 0.06 %wt., respectively (n=26). Ba and Sr are more

216 enriched in the light end member facies (mean values of 0.12 ± 0.16 and 0.11 ± 0.03 %wt.,

217 respectively) relative to the dark end member facies (mean values of 0.04 ± 0.03 and 0.09 ± 0.01

218 %wt., respectively). S, Cr, and Ti are also somewhat elevated in the darker end member facies,

219 but not to a significant level, relative to the lighter intervals.

220 Statistical analysis (n=115; Table S1) shows that most elements exhibit significant correlation

221 with Fe ($p<0.01$), with the exception of Ba, Sr and S. Fe is most strongly correlated with Al

222 ($r=0.86$) and Ca ($r=-0.60$), while the weakest correlations are to Ba ($r=-0.1$), Sr ($r=-0.25$), S

223 ($r=0.24$), P ($r=0.35$), and Ti ($r=0.36$). The latter three correlations are still statistically

224 significant. Sr and Ba significantly correlate ($p<0.01$) to Ca ($r=0.4$ and $r=0.3$) and represent the

225 only elements with a significant positive correlation with Ca. S exhibits weak to no correlation

226 to any other element while P behaves similarly to Zn and Cr ($r=0.5$, $p<0.01$).

227 PCA analysis of the studied interval (Fig. 3) indicates that >55% of the variance could be

228 represented by two principal components. PC1 differentiates Ca, Sr, and Ba vs. Zr, Zn, Fe, Cr,

229 Ti, P, Si and S, whereas PC2 differentiates Ba, Zr, Sr, Fe, and Si vs. Ca, Zn, Cr, Ti, P and S.

230 Facies are aligned along PC1 with the darker organic-rich facies in the positive values and the

231 lighter organic-poor facies on the negative values. At the core level, similar patterns occur

232 when adding the physical properties to the statistical analysis, in which density is aligned along

233 a similar vector as Ba and Sr, while the P-wave velocity behaves similarly to Si and Al.
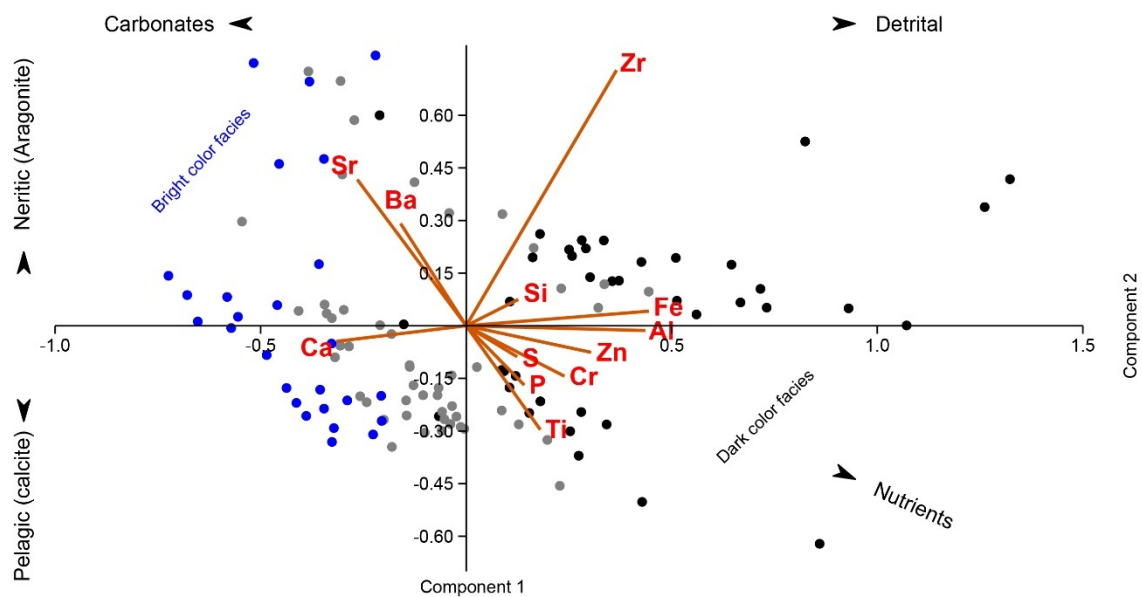
234

235

236

237 *3.3 Lipid biomarkers and Rock-Eval pyrolysis*

238 Biomarkers allow for the identification of sedimentary OM sources as well as the

239 reconstruction of paleo-environmental conditions and the degree of thermal alteration

240 (Eglinton et al., 1964; Summons et al., 2008). We found distinct patterns in lipid distribution

241 associated with the various lithologies identified in core GHPS-1. The *n*-alkanes ranged from

242 *n*-C_{16} to *n*-C_{38} throughout the record (Table S2), with concentrations between 28-711 ng/g and

243 67-3,654 ng/g, for short- (C_{16}-C_{21}) and long-chain (C_{27}-C_{38}) homologues, respectively. The

244 mean value for the average carbon chain length (ACL) of short-chain (C_{16-21}), total *n*-alkanes

245 (C_{16-35}), and long-chain *n*-alkanes (C_{27-35}) was 19 (std dev.=0.3), 24 (std dev.=1.6), and 30 (std

246 dev.=0.4), respectively. The carbon preference index (CPI) of long-chain *n*-alkanes, which

247 portrays the degree of oddity in the different homologues as an indication of OM sources and

248 maturity (Bray and Evans, 1961), ranged between 1.36 and 3.77 (average 2.46, std dev.=0.6;

249 Fig. S5; Table S2). The $C_{27-35}/(C_{27-35}+C_{16-21})$ ratio, used to constrain the relative contribution

250 of terrestrial- and aquatic-derived homologues (Bourbonniere and Meyers, 1996), ranged

251   between 0.9 and 8.8 (average 2.25, std dev.=1.4). The pristane to phytane ratio (Pr/Ph), a proxy

252   for redox (Powell and McKirdy, 1973), ranged between 0.45 and 3.4.

253   We observed facies-specific variations in the distribution of *n*-alkanes, hopanes, and steranes

254   in the GHPS-1 core (Figs. 4, S6, S7, S8). Light-colored chalks were characterized by a high

255   ratio of short- to long-chain *n*-alkanes (Fig. 4), low *n*-alkane concentration, and the absence or

256   low abundance of bacterial hopanes and algal steranes (Fig. 4E). In general, the brown chalk

257   facies lack macro-scale textures related to transport and slumping but show these features on

258   the micro-scale in petrographic slides. These facies is characterized by a lower ratio of short-

259   to long-chain *n*-alkanes, and a high concentration of *n*-alkanes, bacterial hopanes, and algal

260   steranes (Fig. 4A, C). Lastly, the darkest sediments found as filling veins and cavities within

261   the slumped limestones, also associated with very high amounts of transported LBF (i.e.,

262   nummulites), cluster into a third group (Fig. 4B, D). This group is similar to the brown chalks

263   in the sense that they include a high abundance of *n*-alkanes, hopanes, and steranes, although

264   their relative abundances differ (Fig. 4). In particular, whereas we observe sulfur-

265   bond hopanoids (Fig. 5) in the dark MTD-related sediments, they were absent from the brown

266   chalk extracts (Fig. 4A, C, Fig. 5).

267
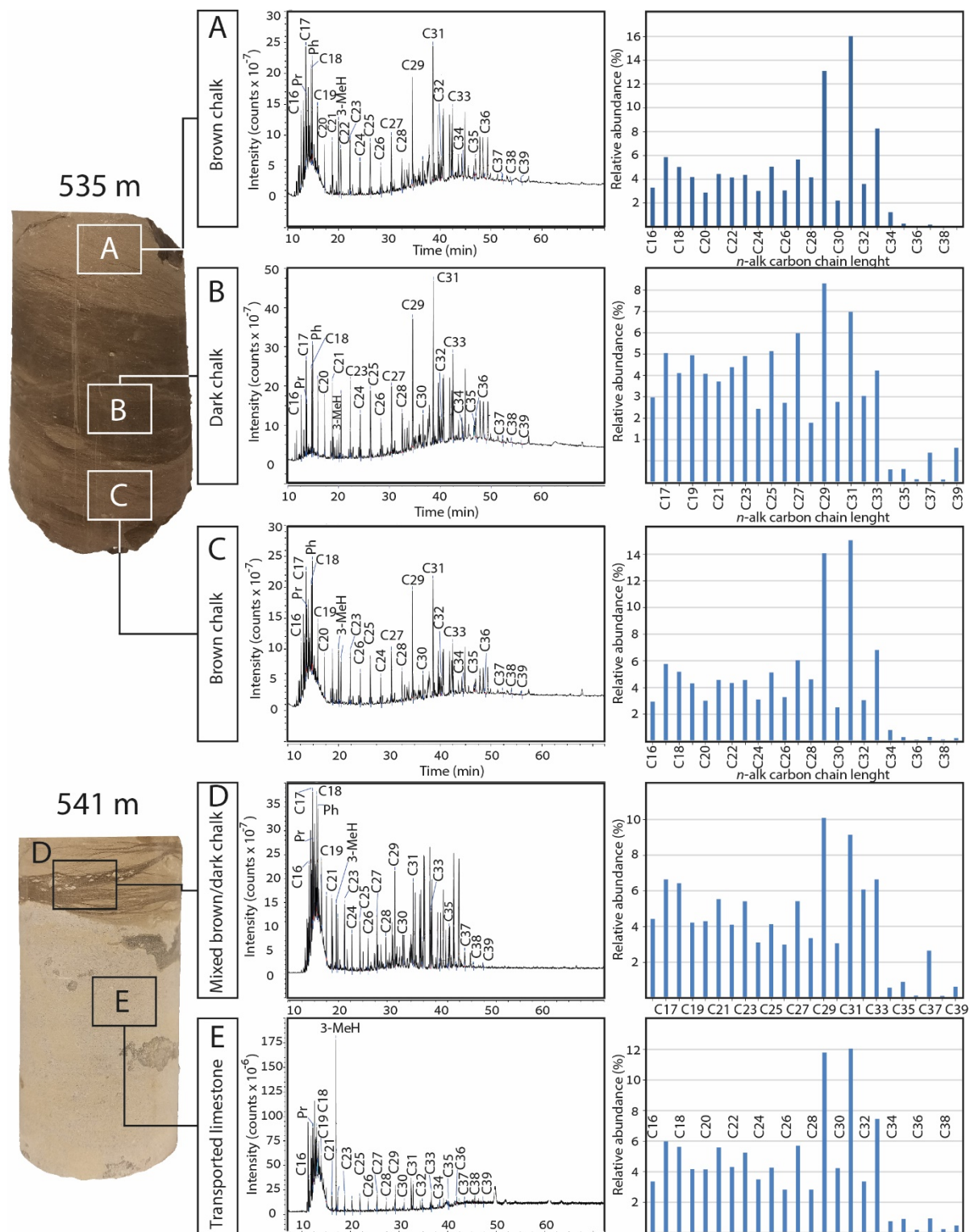
Figure 4. *GC-MS chromatograms of n-alkanes (m/z 57) in 2 representative core samples from the GHPS-1 corehole. Core*
268

samples are displayed on the left, marking the part of the core from which samples were taken (A to E), followed by sample
269

description, extracted ion chromatogram identifying the main n-alkane peaks, followed by plots displaying the relative
270

abundance (proportioned to 100%) of the C_{16} to C_{39} n-alkanes. Pr=pristane; Ph=phytane; 3-MeH=3-MeHenicosane
271

standard. Note the odd-over-even carbon-number predominance of long-chain n-alkanes, the similarity in n-alkane
272

273 *compounds between the brown chalk lithofacies (A and C) relative to the dark chalk lithofacies (B), the combination between*

274 *these two in the mixed lithofacies (D), and the low organic content (as can be deduced from the relative high intensity of the*

275 *3-MeH standard) and distinct n-alkane distribution in the transported limestone lithofacies.*

276   We further observe lithology-bound variations in the relative abundance of selected hopane-

277 and sterane-based thermal maturity and OM source indices (Figs. S7 and S8; (Peters et al.,

278 2005) using Selective Reaction Monitoring (SRM) analysis. Lastly, Rock-Eval pyrolysis

279 indicates average hydrogen index (HI) values between 52 and 656 (average of 492) HC/g TOC,

280 and average oxygen index (OI) values between 32 and 214 (average of 66) CO_2/g TOC (Fig.

281 S9).
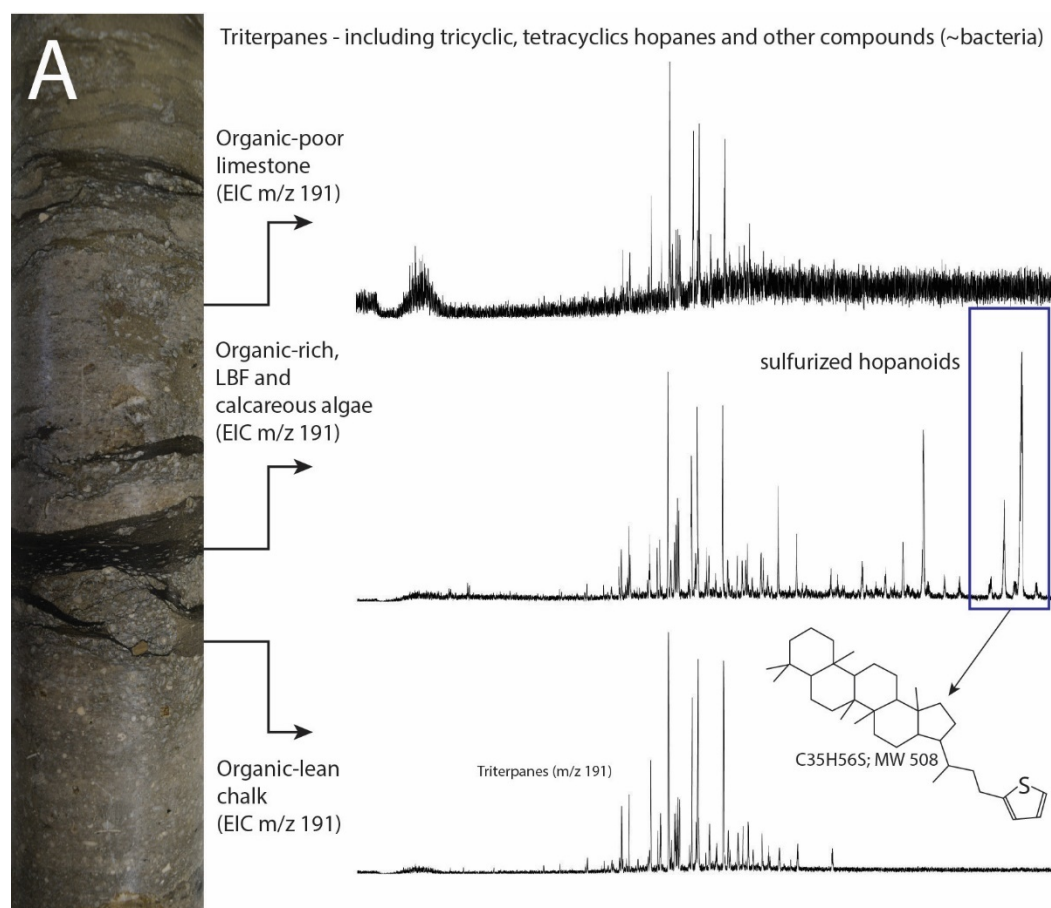
282

283   *Figure 5. Sulfurized hopanoids (blue rectangle in middle chromatogram) seen in the m/z 191 extracted ion chromatogram*

284 *of the thin-grained organic-rich deposits of Facies 5, not identified in the OM extracted from different facies. The identified*

285 *hopanoid molecule containing the sulfurized side chain is drawn and named on the right.*

4. Discussion

287   *4.1 Sedimentary facies of the GHPS-1 core*

288   The greater part of the GHPS-1 core section is composed of limestone units from 5-20 m in

289   thickness, emplaced into dominantly chalky lithofacies units (Fig. 6; Table S3). The limestone

290   units are interpreted as shallow-water components emplaced onto deep-water autochthonous

291   chalks, or onto previously transported para-autochthonous pelagic chalk or limestone. As

292   subunits may include a full spectrum of sediments, including clearly neritic material (including

293   algae and LBF), and fine grain material from the slope, it seems that transport and mixing from

294   different parts of the carbonate system is a major feature in this depositional environment. In

295   most cases the chalky contacts at the base of most subunits, overlying the truncated, at times

296   sheared surface of the previous unit, inform on modes of transport and emplacement. Where

297   displaced material is deposited as thinner horizons a few tens of cm thick that interlaminate

298   with autochthonous chalk, smaller volumes or the thin distal edge of displacement is indicated.

299   Dark, bituminous organic-rich laminae, infillings and veins that characterize the transported

300   limestone facies indicate mobilization of the OM, while lower TOC values in the lighter

301   colored chalky facies onto which the limestone facies are emplaced suggests multiple sources

302   of the OM.
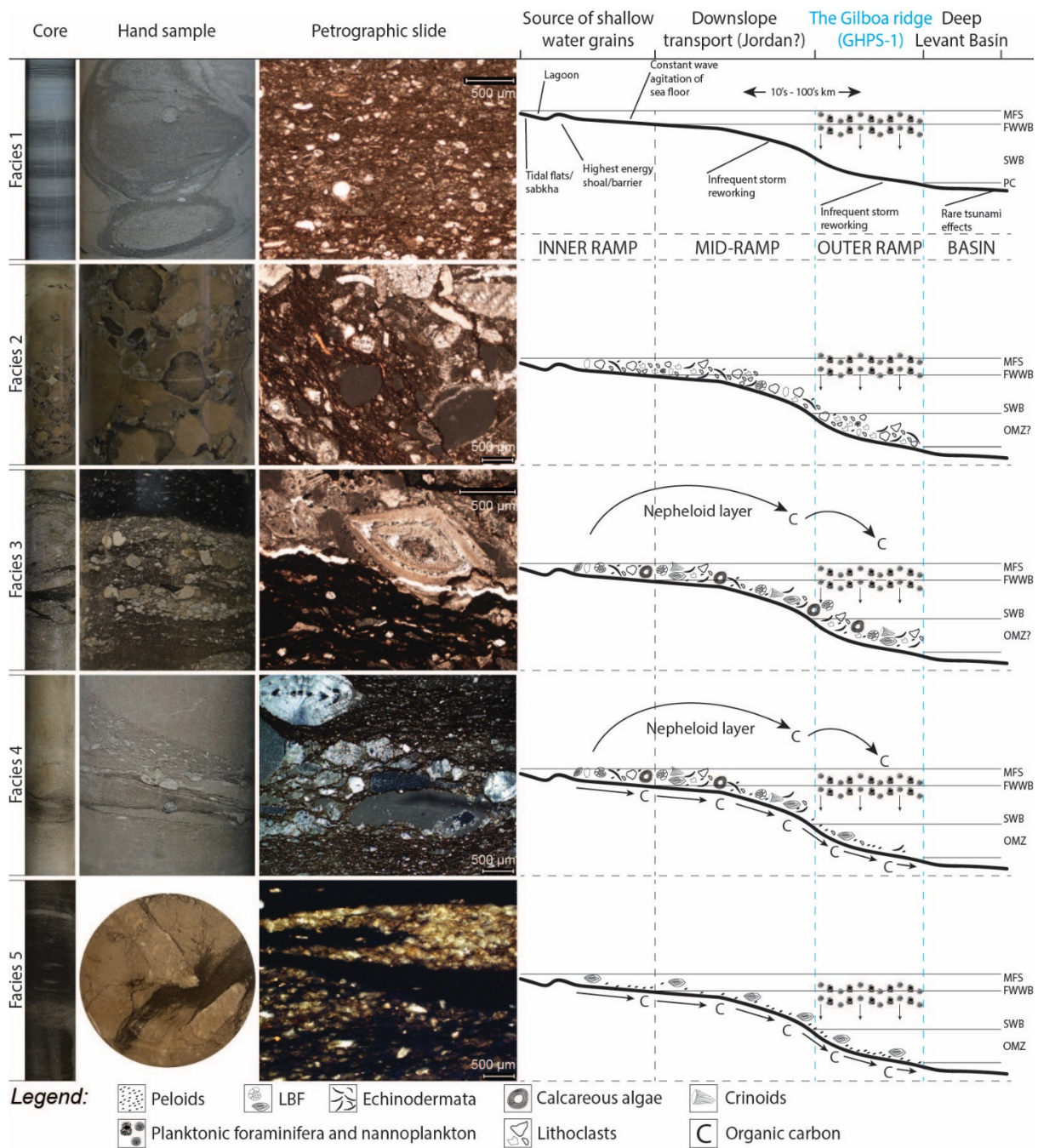
Figure 6. Visual representation of the source and sink of the main facies identified in the Eocene GHPS-1 core from the Gilboa ridge. Elaboration of content description for the variety of facies, from autochthonous to multiphase MTC deposits, characterizing the outer ramp are presented in Table S3. The main environmental subdivision of a homoclinal carbonate ramp broadly follows Burchette and Wright (1992). *MSL = mean sea level; FWWB = fair-weather wave base; SWB = storm wave base; OMZ = oxygen minimum zone. Water depths corresponding to these boundaries are variable but range to 800 m for autochthonous pelagic sediments on the outer ramp (blue). All rock views are vertical cuts, other than the hand sample of facies 5 which is a horizontal cut of a core sample.*

311   Data from the GHPS-1 core indicates a deceptively variable depositional environment
312   throughout the record. The autochthonous facies exhibit a very fine grain and is essentially free
313   of any benthic metazoans. Combined with the planktonic dominance, this would suggest that
314   these rocks were likely deposited in the mesopelagic zone (200-1000 m water depth). Inferring
315   from local paleogeographic reconstructions (Segev et al., 2011; Speijer, 1994), it is suggested
316   that deposition took place in the deeper part of this zone, possibly 600-1000 m water depth.
317   The preservation of LBF in MTCs has been previously documented in the Eocene (Buchbinder
318   et al., 1988), establishing their export into deep water. Similar preservation of LBF in deep
319   water deposits related to MTCs are also reported from the modern (Ash-Mor et al., 2017).
320   Contributions from a variety of shallower depositional environments dominated by LBF, but
321   including pelagic crinoids and other echinoderms, rhodophycean algae and even minor
322   miliolids suggest well-developed depth and energy- based variability in their source region.
323   The mixed provenances of shallow water components within each unit, the absence of bedding
324   within deformed limestone units, the shear features on contacts, and the emplacement on outer-
325   ramp quasi-autochthonous chalk (Figs. 2, 4, 6) indicate that the shallow water components were
326   transported into a deep-water depositional environment. This supposition is also supported by
327   data regarding grain orientation, contact between the grains, and background presence of deep-
328   water open marine components. The outer ramp paleo-position of the depositional environment
329   is supported by petrographic data that show that the chalk intervals are contaminated by fine-
330   grained transported grains from upslope, even during quiescent periods, suggesting lateral
331   proximity and the effects of distal storm activity or contour current redistribution. Lateral
332   transport downslope was followed by diagenetic development and redistribution of OM in
333   pores (Fig. 6; Table S3).
334   The lithologies and sedimentologic textures identified in the GPHS-1 core are grouped into
335   five main facies (Fig. 6; Table S3). Facies 1 represents autochthonous deep-water

336   sedimentation. Facies 2-4 are characterized by modes of introduction of upslope material into

337   the outer ramp depositional environment of the Gilboa region. Facies 2 and 3 are both

338   characterized by episodic slumping of large sediment volumes (possibly even entire blocks in

339   Facies 3). These modes of failure and transport are common and well described in modern

340   carbonate slopes (Etienne et al., 2021; Principaud et al., 2015). They differ in relative

341   abundance and preservation of transported bio- and lithoclasts, which possibly indicates more

342   than one sediment source upslope. Facies 2 is composed of eroded lithoclasts from upslope

343   sources. Facies 3 contains two phases of shallow water components: the matrix with its suite

344   of in-situ microfossils, and the second including large amounts of LBF, calcareous algae,

345   crinoid plates, and indications of microbial binding, together forming hard limestone units

346   bedded within the more autochthonous chalks. The abraded nature of the LBF is a clear

347   downslope transport indicator (Ash-Mor et al., 2017). Facies 4 is a more elaborate

348   conglomeration of upslope components than Facies 3. Cretaceous planktic foraminifera are

349   sometimes recognized among the finer sediments, indicating deep erosion of the slope by mass

350   transport enabling the entrainment of pre-Tertiary sediments along the way. Furthermore,

351   Facies 5 represents the distal part of the toe of the slope, in which transport energy decreases

352   and only the finest transported material reaches the deeper basin. Facies 5 forms thin, intimate

353   interbeds within Facies 1. It can simulate an organic-rich fluid, entering the autochthonous

354   sediment and corroding rims of carbonate clasts. This character is in line with the well

355   described transport of colored dissolved OM downslope, as observed in modern systems (Otis

356   et al., 2004). Transported LBF bioclasts can appear in association with the OM, which fills

357   pores and vugs in the muddy matrix, or as dark laminae interbedded within the chalky sediment.

358   Some of the sedimentological features identified in the GHPS-1 core are known from similar

359   exposed counterparts scattered in the region. Eocene chalks and limestones in the region

360   include a sub-photic autochthonous pelagic chalk facies, possibly indicative of oceanic depths

361 (Benjamini, 1979; Buchbinder et al., 1988). A variety of Eocene limestone lithofacies have

362 been mapped in Israel (Sneh, 1988), often containing large foraminifera as in the GHPS-1 core,

363 with mostly nummulitids and discocyclinids. The sedimentary model for northern Israel of

364 Sneh (1988) proposed that Eocene limestones developed as a reefal facies within the photic

365 zone at a depth of <100. Such a depth will be equivalent to the deep part of a mesophotic zone

366 in oligotrophic settings in the modern (Baldwin et al., 2018). Yet, ubiquitous chalk interbeds

367 were not addressed in this model. Our study indicates that in contrast to Sneh (1988), the

368 shallow-water limestone lithofacies associated with pelagic chalks, more likely represent off-

369 shelf transport, rather than an in-situ reef or shelf-edge deposit. In fact, fully pelagic slumped

370 chalks emplaced within well-bedded pelagic chalks in the southern Shefela Basin (Buchbinder

371 et al., 1988) and elsewhere in Israel, associated with substantial thickness increase (Hatzor et

372 al., 1994), point to continual off-ramp transport during the Eocene also at sub-photic zone

373 depths (Buchbinder et al., 1988) (Figs. S10-S13). However, the GHPS-1 is relatively unique in

374 its organic-richness relative to other time-equivalent sections in the region.

375 *4.2 Inorganic chemistry and physical properties of autochthonous vs. allochthonous*

376 *sediments*

377   Core analyses show a correspondence between lithology and shifts in the measured

378 petrophysical and geochemical values. The homogeneous physical properties expected in a

379 deep-sea chalk lithology is replaced in the GHPS-1 core by highly variable values of P-wave

380 velocity and magnetic susceptibility (Fig. S4). We used a principal component analysis (PCA)

381 to cluster elemental XRF data with TOC, petrophysical measurements, and lithology of the

382 GHPS-1 core. Strong correlation between Fe, Si, and other terrigenous-sourced elements (Fig.

383 3, S14) attests to a strong continental influence. The clustering of high S, P, Cr, and Zn values

384 with organic-rich samples, would correspond to the affinity of micronutrients and natural

385 sulfurization processes to the preservation marine OM. The clustering of elements indicative

386 of continental contribution (i.e., Al, Si, Fe and K), high magnetic susceptibility values, and

387 elevated TOC values in organic-rich samples (Fig. 7), indicates a connection between

388 sedimentary transport and OM accumulation and/or preservation (Figs. S4, S14).
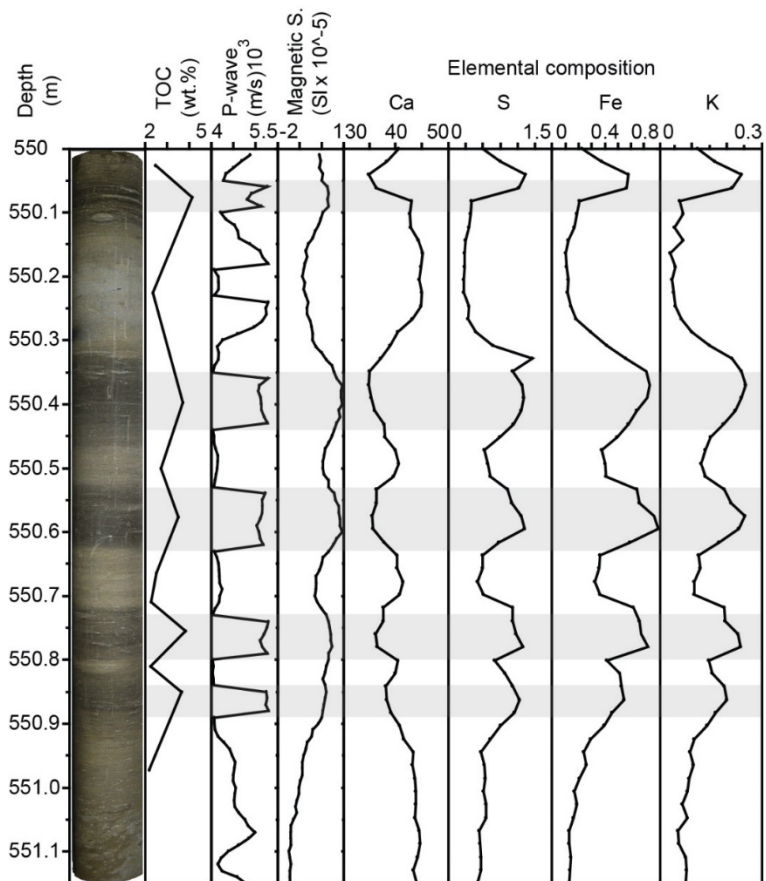
390 *Figure 7. A core interval from the GHPS-1 well (550-551.15 m) showing different organic rich intervals. Dark vs. light*

391 *colored carbonates correspond to 1) shifts in total organic carbon (TOC; 2.2-4.1 wt.%); 2) shifts in the mechanical properties*

392 *of the rock (P-wave velocity; magnetic susceptibility); 3) corresponding shifts in the elemental composition.*

393 The preservation of downslope transported OM (mainly POM) is not trivial. In similar

394 ancient sedimentary settings, it is not uncommon to encounter oxidized "burn-down" OM

395 (Prahl et al., 2003; Wetzel and Uchman, 2018). That is to say, rapidly oxidized by microbial

396 interactions following infiltration of less reduced waters. However, it has been suggested that

397 low bioturbation and high sedimentation rates would contribute to the preservation of OM in

398 MTCs (Wetzel and Uchman, 2001). Evidently, the GHPS-1 core represents a pristine

399   association of transported limestones with distribution, preservation, and burial of un-oxidized

400   OM in marine systems.

4.2 Organic geochemical insights into sources and preservation of organic matter

402   The biomarker, rock-eval pyrolysis, and elemental analyses indicate a strong dependency of

403   OM content and composition on the sedimentary facies. One consistent trait was that while

404   dominantly marine in origin, the OM in the GHPS-1 core includes a combination of both

405   terrigenous and marine OM.

406   We investigated the origin of the OM in the GHPS-1 core based on the identification of both

407   kerogen type and source-specific biomarkers. The pseudo-Van Krevelen diagram of rock-eval

408   data (Fig. S9) shows a wide range of OI values, which suggests variations in oxygenation of

409   the depositional environment, most likely as a result of larger terrigenous input (Espitalie et al.,

410   1977). The pseudo-Van Krevelen diagram indicates that most samples fall between type II

411   (marine/oil prone) and type III (terrestrial/gas prone) kerogen (Dembicki, 2016). The spread of

412   Rock-Eval values across the section might indicate a complex depositional history in this

413   region, with source shifts or the mixing of marine and terrestrial OM from different sources.

414   The higher HI values seen in the samples with TOC >1.5% (Fig. S9) are generally provided by

415   lipid-rich marine sources such as algae, as opposed to the more carbohydrate-rich terrigenous

416   land plants seen in the lower TOC samples (Espitalie et al., 1977; Dembicki, 2016).

417   The wide range of values in the carbon preference index (CPI), the ratio of long- to short-

418   chain *n*-alkanes (LCA/SCA), and the pristane to phytane (Pr/Ph) ratio, all point to mixed

419   sources of OM in the GHPS-1 core (Figs. 4, S5; Table S2). While the Pr/Ph ratio can be affected

420   by the redox potential in the ocean, terrestrial OM can contribute more pristane than phytane

421   due to the preferential oxidation of phytol to phytenic acid (instead of reduction to phytane),

422   and the decarboxylation and reduction to pristane in soils. Consequently, Pr/Ph values <2 might

423   indicate OM deposition in a marine environment, whereas values >3 might indicate a

424   terrigenous OM source (Didyk et al., 1978; Peters et al., 2005). The wide range of Pr/Ph values

425   (0.45-3.4) in the GHPS-1 core is likely to represent the mixing of terrestrial and marine OM in

426   addition to shifts in oxygen content on the seafloor.

427   Furthermore, the distribution of *n*-alkanes, steranes, and hopanes matches the described

428   facies, as follows:

429   1) Light-colored chalks, which are characterized by a low LCA/SCA ratio, low *n*-alkanes

430   concentration, and the absence or very low concentrations of bacterial hopanes and algal

431   steranes (Fig. 4E).

432   2) Brown chalks, which do not include macro-scale textures related to transport and

433   slumping and are characterized by a high LCA/SCA ratio, a high *n*-alkanes concentration,

434   and high concentrations of bacterial hopanes and algal steranes (Fig. 4A, C).

435   3) Brown chalks that include sulfurized hopanoid chains, characterize the darkest sediment

436   units, filling veins and cavities within the slumped limestones, or those associated to high

437   amounts of transported LBF (i.e., nummulites), cluster into a third group similar to that

438   of the brown chalks but also including sulfurized hopanoid chains (Figs. 4D, and 7).

439   The incorporation of sulfur into the molecular structure of biomarkers is commonly observed

440   in reducing environments with abundant sources of reduced sulfur species (e.g., Alsenz et al.,

441   2015). Examples for these settings include sediments of modern upwelling systems (Eglinton

442   et al., 1994; Lückge et al., 1999). Organic matter sulfurization is an important mechanism for

443   the preservation of carbon in reducing environments in the geologic record (Hebting et al.,

444   2006). Several studies propose that OM sulfurization is a key mechanism supporting the

445   extremely high amounts of marine OM preserved in Upper Cretaceous organic-rich sediments

446   in the Levant, reaching 21% TOC (Alsenz et al., 2015; Bein et al., 1990; Meilijson et al., 2018;

447   Rosenberg et al., 2017). The high sulfur content is attributed to the bonding of sulfur with OM

448 in an iron-limited system, in which iron is not available for bonding with the abundant sulfur

449 produced in these environments.

450   Sulfurized compounds in the GHPS-1 core are identified exclusively in Facies 5, from the

451 darkest intervals along the core (Figs. 6, 7, and S6). These dark intervals are interpreted as

452 organic-rich fine grained 'fluids' invading the porous intervals of the limestones of Facies 3,

453 transported from a distal source. The term 'fluids' here is used generally, as these OM-rich

454 deposits may be made of POM, DOM baring fluids or a mixture of DOM and POM.

455 Differentiation is not possible in the lithified samples. We speculate that Facies 5 is a type of

456 distal turbidite deposited during high sedimentation rate periods of fine-grained material at the

457 far end of the toe of the slope (Figs. S1-S3). Here we propose that these upslope- eroded fine-

458 grained sediments originate from older, thermally immature (Meilijson et al., 2018), black

459 shales from Upper Cretaceous outcrops. This scenario is substantiated by the identification of

460 sulfurized hopanes in the facies, possibly fingerprinting it to the underlaying Upper Cretaceous

461 upwelling-related high productivity deposits. These are characterized by a high number of

462 sulfurized compounds – a byproduct of why OM was preserved so well in these deposits

463 (Alsenz et al., 2015; Bein et al., 1990; Meilijson et al., 2018). A more detailed comparison

464 between the sulfur species appearing in facies 5 and those of the organic-rich Upper Cretaceous

465 deposits should be carried out, including sulfur stable isotope analysis.

466   Further evidence supporting the hypothesis that the dark vein-filling organic-rich sediments

467 appearing in facies 5 originate from weathered Upper Cretaceous sediments is provided by

468 several studies from Jordan (Ali Hussein et al., 2015; Alqudah et al., 2014, 2015; Alqudah,

469 Mohammad, Mohammad Ali Hussein, O. Podlaha, 2014; Hakimi et al., 2016; Petrolink et al.,

470 2014). Studies done on the time equivalent section in nearby Jordan indicate the presence of

471 Maastrichtian and Paleocene calcareous nannoplankton and foraminifera suggesting major

472 reworking. The presence of Cretaceous taxa reflects either subaerial erosive input from the

473   hinterland or submarine reworking of Cretaceous strata within the basin (Alqudah et al., 2014).

474   They further state that the highly variable amount of reworked material and associated

475   deposition rates in the basin may represent changes in the tectonic setting during the Eocene.

476   The Gilboa section studied here is located in a distal and deeper depositional setting relative to

477   Jordan. In Jordan, the high abundances of Cretaceous and Palaeocene taxa were interpreted to

478   reflect an increase in accommodation space by active graben flank movements (Alqudah et al.,

479   2014). A dominance of Eocene taxa, on the other hand, was interpreted to indicate either

480   periods of little accommodation space due to graben infill or inversion-type movements of the

481   graben itself. In any case, they conclude, the youngest Eocene and autochthonous taxa

482   represent shallower or low topography graben phases. Here we add another component and

483   hypothesize that within the channel transporting this material, as drilled in the Gilboa ridge,

484   reworking of Cretaceous material includes redeposition of OM from Cretaceous outcrops to

485   transported thinned-grained material in the Eocene, as supported by the presence of sulfurized

486   compounds.

487   The relative contribution of C_{27}, C_{28} and C_{29} steranes, the diagenetic derivatives of algal

488   sterols, is mainly controlled by their biological sources (Brocks et al., 1999; Kodner et al.,

489   2008; Peters et al., 2005). A dominance of C_{27} and C_{28} steranes is generally associated with

490   marine sourced OM, with C_{27} typically indicating a stronger contribution of shallow water red

491   algae, and C_{28} a deeper water diatom-dominated environment, while non-marine OM tends to

492   be dominated by C_{29} sterane precursors (e.g., freshwater green algae or land plants) (Huang

493   and Meinschein, 1979; Peters et al., 2005). However, it should be noted that phylogenetically

494   based surveys of sterol profiles indicate that some green algae produce high abundances of C_{29}

495   relative to C_{27} and C_{28} sterols (Schwark and Empt, 2006).

496   We plotted the relative abundance of $C_{27, 28, 29}$ steranes from 6 analyzed samples from 2 core

497   section, including light and dark sediment intervals, in a ternary plot to assess variations in OM

498   sources (Fig. 8). We found similarities in the distribution of the lighter (organic-lean)

499   sediments, which clustered together closer to the C_{28} endmember relative to the darker

500   (organic-rich) sediments that clustered together and closer to the C_{27} endmember. As with the

501   rock-eval analysis and the *n*-alkanes distribution, it is evident that the lighter and darker

502   sediments differ not only by their degree of organic-richness, but also in the sources of OM.

503   .
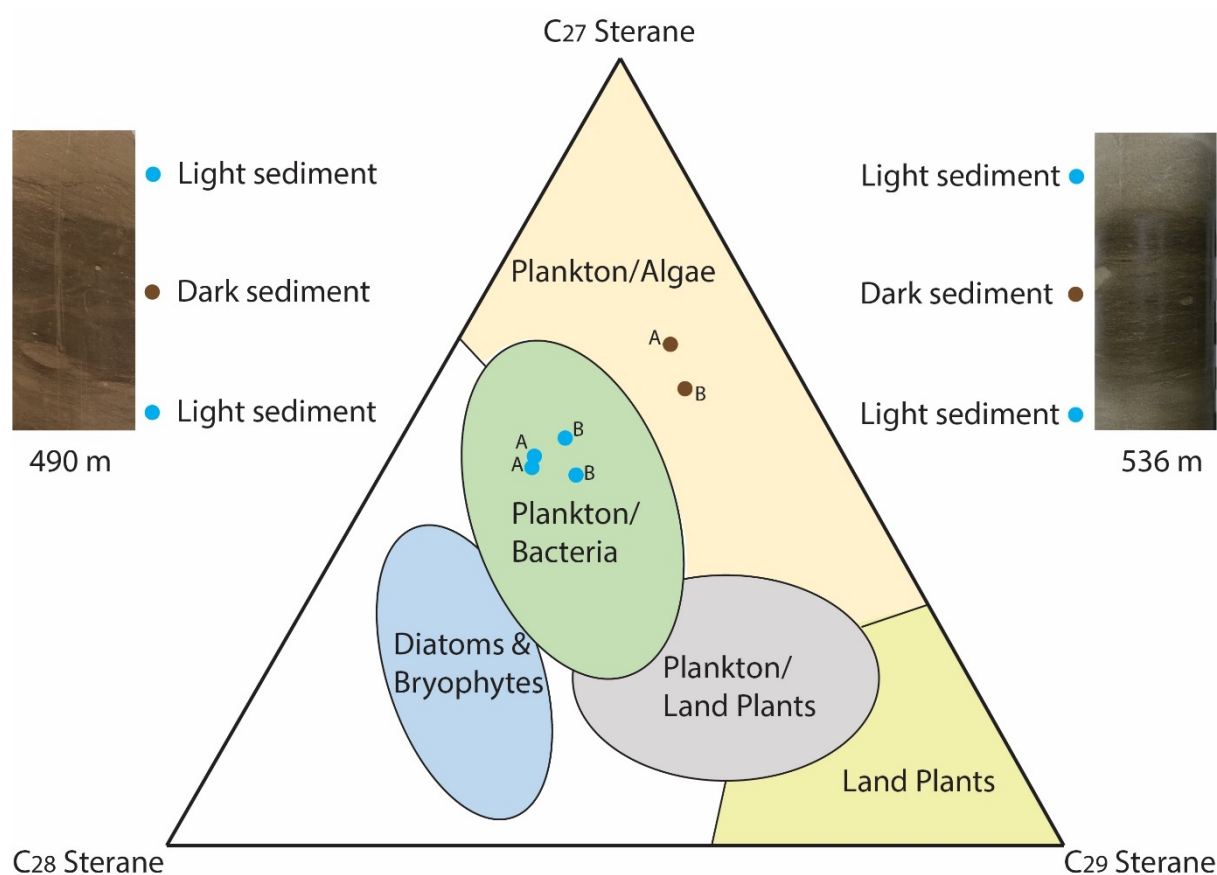
Figure 8. *Distribution of C27, C28, and C29 steranes in the GHPS-1 core samples. End-member sources according to* Huang and Meinschein, (1979) *and Kodner et al. (2008).*

507   In combination, our data indicates mixing of OM sources in the GHPS-1 core, probably

508   because of allochthonous transported sources as well as in-situ production in this outer shelf

509   environment under the influence of an OMZ. This is supported by: (1) Different rock-eval

510   kerogen types, indicating a range of depositional environments sourcing the OM; (2) source-

511   specific (e.g., *n*-alkanes, hopanes) and redox-related (e.g., homohopane index,

512 HHI; $C_{30}norHop/C_{30}Hop$) (Fig. S7), which highlight different OM sources and redox potential

513 between the heavily transported dark sediments and lighter browns; (3) thermal maturity ratios

514 from steranes (e.g., $C_{28}Dia\text{-}S/(S+R)$ and $C_{28}\alpha\alpha\alpha S/(S+R)$) and hopanes ($C_{27}Ts/Tm$, $C_{30}\beta\beta/\alpha\beta$)

515 (Fig. S8), which indicate variations in thermal history. The fact that thermal maturity indicators

516 change with facies and not with stratigraphic depth (as is expected in a sedimentary system

517 buried and exposed to a geothermal gradient over time), indicates the mixing of autochthonous

518 and allochthonous OM sources with varying degrees of maturity into the system (Meilijson et

519 al., 2019; Sepúlveda et al., 2009).

520 *4.4 The search for an analogue model and missing organic carbon sinks*

521 The depositional system we propose here can be visualized as a carbonate version of the

522 present-day Eastern Mediterranean shelf-margin north of the zone of Nilotic clastic input. The

523 correspondence is not to the onshore-nearshore part, but rather to the shelf edge to slope, with

524 the scalloped-like margins and basin fans well offshore. Toe-of-slope deposits thicken

525 considerably at the foot of submarine canyons, with failure and re-deposition from the slope

526 commonly identified in those areas. Although this region is at present mostly a clastic-

527 dominated system, due to post-Eocene regional uplift and the dominance of Nilotic clastic

528 input, the paleophysiographic setting retains elements of the Eocene mud-rich carbonate facies,

529 especially in terms of modes of transport and sediment accumulation. The long-term similarity

530 of these systems is discussed by Schieber et al. (2013). Possible scenarios for the preservation

531 of high amounts of OM include ventilation of reduced layers resulting from local enrichment

532 of biological activity, higher sedimentation rates favoring OM preservation, allochthonous

533 input, and re-deposition of older OM.

534 Organic matter in the marine realm is under constant consumption, be it by burrowing

535 metazoans or oxidation by microbial activity. These activities re-mineralize organic carbon and

536 return it to the dissolved carbon pool of the ocean. Some of this carbon, if released in the

537   sediment, may form authigenic carbonates, binding and lithifying the sediment, and retaining

538   some of that organic carbon. In the case of calcareous MTCs, these also transport aragonite

539   (Droxler et al., 1983). This is evident in our record by the elevated Sr levels, likely sourced

540   from recrystallized aragonite in a relatively closed system (Bialik et al., 2020). The loss of

541   some of the aragonite likely also increased porewater alkalinity and allowed higher rates of

542   preservation (Sulpis et al., 2022). The combined effect likely resulted in the loss of much of

543   the pore-water connectivity and lowered diffusion coefficient. These in turn limited microbial

544   degradation of OM and enhanced preservation.

545   Shelves and upper slope environments are often the most productive regions of the ocean,

546   yet much of that organic carbon is not preserved in the sedimentary record (Emerson and

547   Hedges, 2008). The sedimentological transport mechanism reported here for the Eocene

548   illustrates a highly efficient organic carbon burial mode that is in line with those observed in

549   the modern (Benner et al., 2005; Biscara et al., 2011; Fichot and Benner, 2014). This

550   mechanism (i.e., entrapment and rapid burial of OM by mass wasting events) might have been

551   more efficient in the early Eocene, when deep and intermediate water masses where less

552   ventilated (Thomas et al., 2010). High burial rate has long been considered as important to the

553   preservation of OM, notably POM. However, the movement of suspended material during mass

554   wasting events opens the possibility to additionally trapping DOM, notably any that may be

555   present in or just above the benthic boundary layer.

556   The absence of bioturbation and metazoans in the GHPS-1 core point to low oxygen

557   availability near the seafloor (also in agreement with the low Pr/Ph ratio), supporting the notion

558   of less ventilated, sluggish, deep to intermediate water masses. Thus, in view of the potential

559   for efficient organic carbon sequestration, the debate regarding higher Early Eocene degassing

560   or lower organic burial efficiency (Komar et al., 2013) is somewhat swayed towards the former.

561   The findings from the GHPS-1 core are relevant not only to the Eocene but represent the

562   termination of a 40 Myr period of high productivity and upwelling in the NW Arabian margin

563   from the Santonian to the Eocene (Meilijson et al., 2014, 2019). On a global scale, this study

564   highlights the importance of transport systems in the delivery and burial of OM from

565   productive and oligotrophic near-shore environments to deep marine settings where it can be

566   permanently sequestered. Examples for transport of near-shore components and OM to

567   deeper setting include the Eocene graphoglyptids-bearing organic-rich turbidites in Argentina

568   (Olivero et al., 2010), turbidites as the principal mechanism yielding black shales in the early

569   deep Atlantic Ocean (Degens et al., 1986), organic-rich turbidites within pelagic clay

570   sequences from the Cape Verde Abyssal Plain in the NE Atlantic (Robinson, 2001), among

571   others.

572   A full quantitative estimation of the impact of this transport mechanism on carbon burial

573   within the scope of this study is not possible given the large uncertainties in many of the

574   parameters. However, to get a sense of it we propose the following thought exercise. We use

575   an Early Eocene shelf area (A) of ~1.2×10^{14} m^2 (Cao et al., 2017), a shelf sedimentation

576   rate (SSR) of between 0.1 and 1 cm/yr, an average density (ρ) of 1.7 g/cm^3 (Tenzer and

577   Gladkikh, 2014), and an organic carbon content (OCC) in sediment of between 0.05% and

578   0.20%. Using equation 1:

579   (1) $OCPP = A \times SSR \times \rho \times OCC$

580   Consequently, the potential pool of organic carbon (OCPP) to be preserved at the time

581   would have been between 1.02×10^{14} to 4.08×10^{15} gr C per year on the shelves. This

582   would place Eocene organic carbon burial rates on par with (and likely lower) that of the

583   warmest parts of the Miocene at ~10^{15} gr C per year (Li et al., 2023). Organic matter

584   generation in the ocean is not uniformly distributed but instead focused on specific locations

585   such as river mouths and upwelling zones, where sedimentation rate and TOC are high. As

586 such the potential to mobilize through this mechanism large quantities of organic carbon is

587 significant, making the higher estimate more probable. That said, there is still much to be

588 improved in the parameterization. We call on the community to consider the potential impact

589 of this mechanism and improve the state of knowledge to better understand and quantify it.

590 **5. Conclusions**

591 • The lithologies identified in the GHPS-1 core from northern Israel are predominantly

592 of carbonate type. The carbonate sources are mainly autochthonous pelagic, with

593 additional sources ranging from para-autochthonous materials accumulated on the

594 slope, to sources on various parts of the oligophotic outer to mid-ramp carbonate

595 system characterized by larger benthic foraminifera, calcareous algae, and OM.

596 • The mix of lithologies present in the GHPS-1 core likely indicates mass transport in

597 the form of slides and slumps of partially lithified or un-lithified mud, including

598 lithoclasts, slurries and turbidites. Transport entrains material present on the slope

599 including erosion and reworking of material from as old as the Cretaceous.

600 • Elemental and magnetic susceptibility analyses indicate that the material contains

601 both allochthonous (land-derived) and autochthonous (marine-derived) trace

602 elements.

603 • A detailed characterization of the OM based on lipid biomarkers, rock-eval pyrolysis,

604 and elemental analyses, indicates the mixing of different types or OM. This is

605 demonstrated by a mixing of type II and type II-III kerogens, *n*-alkanes showing

606 variations in terrestrial vs. aquatic sources, the carbon preference index (CPI) of n-

607 alkanes values (a proxy for biological sources and thermal maturity), the

608 pristane/phytane (Pr/Ph) ratio (a proxy for redox conditions), the relative abundances

609 and types of bacterial hopanes and algal steranes, the occurrence of sulfurized

hopanoids in one of the transported facies, and the differences in thermal maturity. In combination, sedimentological, physical, and elemental analyses indicate shifts between autochthonous and allochthonous sedimentation, whereas statistical analysis (PCA) of the inorganic geochemical record reveals a repeatable correlation between modes of sedimentation and preservation/composition of OM. It seems that organic richness increases within intervals of allochthonous sedimentation.

- Organic matter preservation is enhanced in poor oxygenated seafloor conditions, but most likely also points to the rapid burial beneath mass-transport deposits. Horizons rich in OM may be derived from three different sources: OM with a stronger fingerprint of terrestrial sources (e.g., abundant plant leaf waxes) transported from terrestrial and nearshore environments; a stronger marine fingerprint with sulfurized hopanoid side chains which seem to be reworked from pre-existing, organic-rich, immature Cretaceous carbonates entrained within fined-grained distal turbidites in the para-autochthonous facies; and productivity-derived OM deposited on the sea floor of the deep marine environment.

- The depositional model we propose here can be visualized as a modified, carbonate-dominated version of the present-day Eastern Mediterranean shelf-margin outside of the main zone of Nilotic clastic input. The onshore-nearshore part was heavily modified by post-Eocene uplift, but the shelf edge to slope part, with scalloped margins, basin fans, channels, and transport conduits well offshore, retains many Eocene features to the present.

- This study highlights the importance of transport systems in the delivery and burial of OM from productive and oligotrophic near-shore settings to its long-term sequestration in deep marine environments. We generally calculate that for the Early Eocene, allowing for only 0.1‰ of shelf carbon to be preserved through transport by

635   the MTD mechanism would account for between 0.3% to 13.7% of all organic carbon

636   burial.

637   • Possible scenarios for the preservation of high amounts of OM include ventilation of

638   reduced layers resulting with local enrichment of biological activity, higher

639   sedimentation rates due to offshore transport favoring OM preservation, transported

640   OM, and re-deposition of older OM. We show how transport mechanisms allow for

641   the long-term burial of organic carbon in marine systems in the geological record.

642   When taking into consideration similar processes reported to occur around the world

643   today, it is clear that transport and long-term burial of organic carbon in marine

644   systems is a fundamental part of the global carbon cycle, which has been shaping our

645   planet throughout the geological record. This notion should be implemented in

646   modeling and quantification of the carbon cycle throughout Earth history.

Acknowledgments

References

658   Ali Hussein, M. A., Alqudah, M., Blessenohl, M., Podlaha, O. G., & Mutterlose, J. (2015).

659   Depositional environment of Late Cretaceous to Eocene organic-rich marls from Jordan.

660   *GeoArabia*, *20*(1), 191–210.

661   Alqudah, M., Ali Hussein, M., van den Boorn, S., Giraldo, V. M., Kolonic, S., Podlaha, O.

662   G., & Mutterlose, J. (2014). Eocene oil shales from jordan - paleoenvironmental

663   implications from reworked microfossils. *Marine and Petroleum Geology*, *52*, 93–106.

664   https://doi.org/10.1016/j.marpetgeo.2014.02.001

665   Alqudah, M., Ali Hussein, M., van den Boorn, S., Podlaha, O. G., & Mutterlose, J. (2015).

666   Biostratigraphy and depositional setting of Maastrichtian - Eocene oil shales from

667   Jordan. *Marine and Petroleum Geology*, *60*(February), 87–104.

668   https://doi.org/10.1016/j.marpetgeo.2014.07.025

669   Alqudah, Mohammad, Mohammad Ali Hussein, O. Podlaha, J. M. (2014). Calcareous

670   nannofossil biostratigraphy of Eocene oil shales from central Jordan. *Geoarabia -*

671   *ManamaManama*, *19*(1), 117–140.

672   Alsenz, H., Illner, P., Ashckenazi-Polivoda, S., Meilijson, A., Abramovich, S., Feinstein, S.,

673   Almogi-Labin, A., Berner, Z., Püttmann, W., 2015. Geochemical evidence for the link

674   between sulfate reduction, sulfide oxidation and phosphate accumulation in a Late

675   Cretaceous upwelling system. Geochem Trans 16, 1–13. https://doi.org/10.1186/s12932-

676   015-0017-1

677   Amante, C., Eakins, B.W., 2009. ETOPO1 1 Arc-Minute Global Relief Model: Procedures,

678   Data Sources and Analysis. NOAA Technical Memorandum NESDIS NGDC-24.

679   https://doi.org/10.1594/PANGAEA.769615

680   Ash-Mor, A., Bookman, R., Kanari, M., Ben-Avraham, Z., Almogi-Labin, A., 2017.

681   Micropaleontological and taphonomic characteristics of mass transport deposits in the

682   northern Gulf of Eilat/Aqaba, Red Sea. Mar Geol 391.

683   https://doi.org/10.1016/j.margeo.2017.07.009

684   Baldwin, C.C., Tornabene, L., Robertson, D.R., 2018. Below the Mesophotic. Sci Rep 8.

685   https://doi.org/10.1038/s41598-018-23067-1

686   Barrõn, C., Duarte, C.M., 2015. Dissolved organic carbon pools and export from the coastal

687   ocean. Global Biogeochem Cycles 29. https://doi.org/10.1002/2014GB005056

688   Bauer, J.E., Druffel, E.R.M., 1998. Ocean margins as a significant source of organic matter to

689   the deep open ocean. Nature 392, 20–23. https://doi.org/10.1038/33122

690   Bein, A., Almogi-Labin, A., Sass, E., 1990. Sulfur Sinks and Organic-Carbon Relationships

691   in Cretaceous Organic-Rich Carbonates - Implications for Evaluation of Oxygen-Poor

692   Depositional-Environments. Am J Sci 290, 882–911.

693   Benjamini, C., 1979. Facies relationships in the Avedat Group (Eocene) in the Northern

694   Negev, Israel. Isr. J. Earth-Sci. 28.

695   Benner, R., Louchouarn, P., Amon, R.M.W., 2005. Terrigenous dissolved organic matter in

696   the Arctic Ocean and its transport to surface and deep waters of the North Atlantic.

697   Global Biogeochem Cycles 19. https://doi.org/10.1029/2004GB002398

698   Bialik, O.M., Bookman, R., Elyashiv, H., Marietou, A., Saar, R., Rivlin, T., Taha, N.,

699   Benaltabet, T., Lotem, N., Funaro, E., Antler, G., 2022. Tropical storm-induced

700   disturbance of deep-water porewater profiles, Gulf of Aqaba. Mar Geol 453.

701   https://doi.org/10.1016/j.margeo.2022.106926

702   Bialik, O.M., Reolid, J., Betzler, C., Eberli, G.P., Waldmann, N.D., 2020. Source shifts to

703   periplatform deposits during the early to middle Miocene in response to climatic and

704   oceanographic forcing, Maldives, western Indian Ocean. Palaeogeogr Palaeoclimatol

705   Palaeoecol 559. https://doi.org/10.1016/j.palaeo.2020.109969

706   Bianchi, T.S., Cui, X., Blair, N.E., Burdige, D.J., Eglinton, T.I., Galy, V., 2018. Centers of

707   organic carbon burial and oxidation at the land-ocean interface. Org Geochem.

708   https://doi.org/10.1016/j.orggeochem.2017.09.008

709   Biscara, L., Mulder, T., Martinez, P., Baudin, F., Etcheber, H., Jouanneau, J.M., Garlan, T.,

710   2011. Transport of terrestrial organic matter in the Ogooué deep sea turbidite system

711   (Gabon). Mar Pet Geol 28. https://doi.org/10.1016/j.marpetgeo.2010.12.002

712   Blair, N.E., Aller, R.C., 2012. The fate of terrestrial organic carbon in the Marine

713   environment. Ann Rev Mar Sci 4. https://doi.org/10.1146/annurev-marine-120709-

714   142717

715   Boudinot, F.G., Sepúlveda, J., 2020. Marine organic carbon burial increased forest fire

716   frequency during Oceanic Anoxic Event 2. Nat Geosci 13.

717   https://doi.org/10.1038/s41561-020-0633-y

718   Bourbonniere, R.A., Meyers, P.A., 1996. Sedimentary geolipid records of historical changes

719   in the watersheds and productivities of Lakes Ontario and Erie. Limnol Oceanogr 41.

720   https://doi.org/10.4319/lo.1996.41.2.0352

721   Bray, E.E., Evans, E.D., 1961. Distribution of n-paraffins as a clue to recognition of source
722   beds. Geochim Cosmochim Acta 22, 2–15. https://doi.org/10.1016/0016-
723   7037(61)90069-2

724   Brocks, J.J., Logan, G.A., Buick, R., Summons, R.E., 1999. Archean molecular fossils and
725   the early rise of eukaryotes. Science (1979).
726   https://doi.org/10.1126/science.285.5430.1033

727   Buchbinder, B., Benjamini, C., Mimran, Y., Gvirtzman, G., 1988. Mass transport in Eocene
728   pelagic chalk on the northwestern edge of the Arabian platform, Shefela area, Israel.
729   Sedimentology 35, 257–274. https://doi.org/10.1111/j.1365-3091.1988.tb00948.x

730   Burchette, T.P., Wright, V.P., 1992. Carbonate ramp depositional systems. Sediment Geol 79,
731   3–57. https://doi.org/10.1016/0037-0738(92)90003-A

732   Canals, M., Puig, P., de Madron, X.D., Heussner, S., Palanques, A., Fabres, J., 2006.
733   Flushing submarine canyons. Nature 444, 354–357. https://doi.org/10.1038/nature05271

734   Cao, W., Zahirovic, S., Flament, N., Williams, S., Golonka, J., Dietmar Müller, R., 2017.
735   Improving global paleogeography since the late Paleozoic using paleobiology.
736   Biogeosciences 14. https://doi.org/10.5194/bg-14-5425-2017

737   Chen, F., Lu, X., Song, Z., Huang, C., Jin, G., Chen, C., Zhou, X., Lao, Q., Zhu, Q., 2021.
738   Coastal currents regulate the distribution of the particulate organic matter in western
739   Guangdong offshore waters as evidenced by carbon and nitrogen isotopes. Mar Pollut
740   Bull 172. https://doi.org/10.1016/j.marpolbul.2021.112856

741   Coleman, J.M., Prior, D.B., 1988. Mass wasting on continental margins. Annu Rev Earth
742   Planet Sci 16, 19.

743   Degens, E.T., Emeis, K.C., Mycke, B., Wiesner, M.G., 1986. Turbidites, the principal
744   mechanism yielding black shales in the early deep Atlantic Ocean. Geol Soc Spec Publ
745   21. https://doi.org/10.1144/GSL.SP.1986.021.01.26

746   Dembicki, H., 2016. Practical Petroleum Geochemistry for Exploration and Production,
747   Elsevier.

748   Didyk, B.M., Simoneit, B.R.T., Brassell, S.C., Eglinton, G., 1978. Organic geochemical
749   indicators of palaeoenvironmental conditions of sedimentation. Nature 272, 216–222.
750   https://doi.org/10.1038/272216a0

751   Droxler, A.W., Schlager, W., Whallon, C.C., 1983. Quaternary aragonite cycles and oxygen-
752   isotope record in Bahamian carbonate ooze. Geology 11. https://doi.org/10.1130/0091-
753   7613(1983)11<235:QACAOR>2.0.CO;2

754 Eglinton, G., Scott, P.M., Belsky, T., Burlingame, A.L., Calvin, M., 1964. Hydrocarbons of
755   biological origin from a one-billion-year-old sediment. Science (1979) 145.
756   https://doi.org/10.1126/science.145.3629.263

757 Eglinton, T.I., Galy, V. V., Hemingway, J.D., Feng, X., Bao, H., Blattmann, T.M., Dickens,
758   A.F., Gies, H., Giosan, L., Haghipour, N., Hou, P., Lupker, M., McIntyre, C.P.,
759   Montluçon, D.B., Peucker-Ehrenbrink, B., Ponton, C., Schefuß, E., Schwab, M.S., Voss,
760   B.M., Wacker, L., Wu, Y., Zhao, M., 2021. Climate control on terrestrial biospheric
761   carbon turnover. Proc Natl Acad Sci U S A 118.
762   https://doi.org/10.1073/pnas.2011585118

763 Eglinton, T.I., Irvine, J.E., Vairavamurthy, A., Zhou, W., Manowitz, B., 1994. Formation and
764   diagenesis of macromolecular organic sulfur in Peru margin sediments. Org Geochem
765   22, 781–799. https://doi.org/10.1016/0146-6380(94)90139-2

766 Embley, R.W., 1980. The role of mass transport in the distribution and character of deep-
767   ocean sediments with special reference to the North Atlantic. Mar Geol 38, 23–50.
768   https://doi.org/10.1016/0025-3227(80)90050-X

769 Emerson, S., Hedges, J., 2008. Chemical oceanography and the marine carbon cycle,
770   Chemical Oceanography and the Marine Carbon Cycle.
771   https://doi.org/10.1017/CBO9780511793202

772 Espitalie, J., Madec, M., Tissot, B., Mennig, J.J., Leplat, P., 1977. Source Rock
773   Characterization Method for Petroleum Exploration, in: Offshore Technology
774   Conference. Houston, pp. 439–444. https://doi.org/10.4043/2935-ms

775 Etienne, S., Le Roy, P., Tournadour, E., Roest, W.R., Jorry, S., Collot, J., Patriat, M.,
776   Largeau, M.A., Roger, J., Clerc, C., Dechnick, B., Sanborn, K.L., Lepareur, F.,
777   Horowitz, J., Webster, J.M., Gaillot, A., 2021. Large-scale margin collapses along a
778   partly drowned, isolated carbonate platform (Lansdowne Bank, SW Pacific Ocean). Mar
779   Geol 436. https://doi.org/10.1016/j.margeo.2021.106477

780 Evans, D., Harrison, Z., Shannon, P.M., Laberg, J.S., Nielsen, T., Ayers, S., Holmes, R.,
781   Hoult, R.J., Lindberg, B., Haflidason, H., Long, D., Kuijpers, A., Andersen, E.S., Bryn,
782   P., 2005. Palaeoslides and other mass failures of Pliocene to Pleistocene age along the
783   Atlantic continental margin of NW Europe. Mar Pet Geol 22, 1131–1148.
784   https://doi.org/10.1016/j.marpetgeo.2005.01.010

785 Fichot, C.G., Benner, R., 2014. The fate of terrigenous dissolved organic carbon in a river-
786   influenced ocean margin. Global Biogeochem Cycles 28.
787   https://doi.org/10.1002/2013GB004670

788 Flugel, E., 2010. Microfacies of Carbonate Rocks. Springer.
789   https://doi.org/10.1017/CBO9781107415324.004

790 Frey-Martinez, J., Cartwright, J., Hall, B., 2005. 3D seismic interpretation of slump
791   complexes: examples from the continental margin of Israel. Basin Research 17, 83–108.
792   https://doi.org/10.1111/j.1365-2117.2005.00255.x

793 Hakimi, M. H., Abdullah, W. H., Alqudah, M., Makeen, Y. M., & Mustapha, K. A. (2016).
794   Organic geochemical and petrographic characteristics of the oil shales in the Lajjun area,
795   Central Jordan: Origin of organic matter input and preservation conditions. *Fuel*, *181*,
796   34–45. https://doi.org/10.1016/j.fuel.2016.04.070

797 Hammer, Ø., Harper, D.A.T., Ryan, P.D., 2001. Paleontological statistics software package
798   for education and data analysis. Palaeontologia Electronica 4, 9–18.
799   https://doi.org/10.1016/j.bcp.2008.05.025

800 Hatzor, Y., Benjamini, C., Mimran, Y., Grossowicz, L.P., 1994. The Eocene stratigraphy of
801   Mt. Gilboa and northern Samaria, Israel. Israel Journal of Earth Sciences.

802 Hebting, Y., Schaeffer, P., Behrens, A., Adam, P., Schmitt, G., Schneckenburger, P.,
803   Bernasconi, S.M., Albrecht, P., 2006. Biomarker evidence for a major preservation
804   pathway of sedimentary organic carbon. Science (1979) 312.
805   https://doi.org/10.1126/science.1126372

806 Huang, W.Y., Meinschein, W.G., 1979. Sterols as ecological indicators. Geochim
807   Cosmochim Acta. https://doi.org/10.1016/0016-7037(79)90257-6

808 Inthorn, M., Mohrholz, V., Zabel, M., 2006. Nepheloid layer distribution in the Benguela
809   upwelling area offshore Namibia. Deep Sea Research Part I: Oceanographic Research
810   Papers 53, 1423–1438. https://doi.org/10.1016/j.dsr.2006.06.004

811 Kodner, R.B., Pearson, A., Summons, R.E., Knoll, A.H., 2008. Sterols in red and green algae:
812   Quantification, phylogeny, and relevance for the interpretation of geologic steranes.
813   Geobiology. https://doi.org/10.1111/j.1472-4669.2008.00167.x

814 Komar, N., Zeebe, R.E., Dickens, G.R., 2013. Understanding long-term carbon cycle trends:
815   The late Paleocene through the early Eocene. Paleoceanography 28.
816   https://doi.org/10.1002/palo.20060

817   Li, Z., Zhang, Y.G., Torres, M., Mills, B.J.W., 2023. Neogene burial of organic carbon in the
818   global ocean. Nature 613, 90–95. https://doi.org/10.1038/s41586-022-05413-6

819   Lückge, A., Ercegovac, M., Strauss, H., Littke, R., 1999. Early diagenetic alteration of
820   organic matter by sulfate reduction in Quaternary sediments from the northeastern
821   Arabian Sea. Mar Geol 158, 1–13. https://doi.org/10.1016/S0025-3227(98)00191-1

822   Meilijson, A., Ashckenazi-Polivoda, S., Illner, P., Speijer, R.P., Almogi-Labin, A., Feinstein,
823   S., Püttmann, W., Abramovich, S., 2018. From phytoplankton to oil shale reservoirs: A
824   19-million-year record of the Late Cretaceous Tethyan upwelling regime in the Levant
825   Basin. Mar Pet Geol 95, 188–205. https://doi.org/10.1016/j.marpetgeo.2018.04.012

826   Meilijson, A., Hilgen, F., Sepúlveda, J., Steinberg, J., Fairbank, V., Flecker, R., Waldmann,
827   N.D., Spaulding, S.A., Bialik, O.M., Boudinot, F.G., Illner, P., Makovsky, Y., 2019.
828   Chronology with a pinch of salt: Integrated stratigraphy of Messinian evaporites in the
829   deep Eastern Mediterranean reveals long-lasting halite deposition during Atlantic
830   connectivity. Earth Sci Rev 194, 374–398.
831   https://doi.org/10.1016/j.earscirev.2019.05.011

832   Olivero, E.B., López C., M.I., Malumián, N., Torres Carbonell, P.J., 2010. Eocene
833   graphoglyptids from shallow-marine, highenergy, organic-rich, and bioturbated
834   turbidites, Fuegian Andes, Argentina. Acta Geologica Polonica 60.

835   Otis, D.B., Carder, K.L., English, D.C., Ivey, J.E., 2004. CDOM transport from the Bahamas
836   Banks. Coral Reefs 23. https://doi.org/10.1007/s00338-003-0356-8

837   Peters, K.E., 1986. Guidelines for Evaluating Petroleum Source Rock Using Programmed
838   Pyrolysis. American Association of Petroleum Geologists Bulletin 70, 318–329.
839   https://doi.org/10.1306/94885688-1704-11D7-8645000102C1865D

840   Peters, K.E., Walters Clifford C, Moldowan, J.M., 2005. The Biomarker Guide, Biomarkers
841   and Isotopes in Petroleum Exploration and Earth Histroy, Volume 2. Cambridge.
842   https://doi.org/10.1017/s0016756806212056

843   Petrolink, G., Alqudah, M., Hussein, M. A., Podlaha, O. G., Van Den Boorn, S., Kolonic, S.,
844   & Mutterlose, J. (2014). *Calcareous nannofossil biostratigraphy of Eocene oil shales*
845   *from central Jordan* (Vol. 19, Issue 1).

846   Powell, T.G., McKirdy, D.M., 1973. Relationship between Ratio of Pristane to Phytane,
847   Crude Oil Composition and Geological Environment in Australia. Nature Physical
848   Science 243. https://doi.org/10.1038/physci243037a0

849   Prahl, F.G., Cowie, G.L., de Lange, G.J., Sparrow, M.A., 2003. Selective organic matter
850   preservation in "burn-down" turbidites on the Madeira Abyssal Plain. Paleoceanography
851   18. https://doi.org/10.1029/2002pa000853

852   Principaud, M., Mulder, T., Gillet, H., Borgomano, J., 2015. Large-scale carbonate submarine
853   mass-wasting along the northwestern slope of the Great Bahama Bank (Bahamas):
854   Morphology, architecture, and mechanisms. Sediment Geol 317.
855   https://doi.org/10.1016/j.sedgeo.2014.10.008

856   Regnier, P., Resplandy, L., Najjar, R.G., Ciais, P., 2022. The land-to-ocean loops of the
857   global carbon cycle. Nature. https://doi.org/10.1038/s41586-021-04339-9

858   Robinson, S.G., 2001. Early diagenesis in an organic-rich turbidite and pelagic clay sequence
859   from the Cape Verde Abyssal Plain, NE Atlantic: Magnetic and geochemical signals.
860   Sediment Geol 143. https://doi.org/10.1016/S0037-0738(00)00187-1

861   Rosenberg, Y.O., Meshoulam, A., Said-Ahmad, W., Shawar, L., Dror, G., Reznik, I.J.,
862   Feinstein, S., Amrani, A., 2017. Study of thermal maturation processes of sulfur-rich
863   source rock using compound specific sulfur isotope analysis. Org Geochem 112.
864   https://doi.org/10.1016/j.orggeochem.2017.06.005

865   Schieber, J., Southard, J.B., Kissling, P., Rossman, B., Ginsburg, R., 2013. Experimental
866   Deposition of Carbonate Mud From Moving Suspensions: Importance of Flocculation
867   and Implications For Modern and Ancient Carbonate Mud Deposition. Journal of
868   Sedimentary Research 83, 1025–1031. https://doi.org/10.2110/jsr.2013.77

869   Schwark, L., Empt, P., 2006. Sterane biomarkers as indicators of palaeozoic algal evolution
870   and extinction events. Palaeogeogr Palaeoclimatol Palaeoecol 240, 225–236.
871   https://doi.org/10.1016/j.palaeo.2006.03.050

872   Segev, A., Schattner, U., Lyakhovsky, V., 2011. Middle-Late Eocene structure of the
873   southern Levant continental margin - Tectonic motion versus global sea-level change.
874   Tectonophysics 499, 165–177. https://doi.org/10.1016/j.tecto.2011.01.006

875   Sepúlveda, J., Wendler, J.E., Summons, R.E., Hinrichs, K., 2009. Rapid Resurgence of
876   Marine Productivity After the Cretaceous-Paleogene Mass Extinction. Science (1979)
877   326, 129–132. https://doi.org/10.1126/science.1176233

878   Shanmugam, G., 2000. 50 years of the turbidite paradigm (1950s-1990s): Deep-water
879   processes and facies models-a critical perspective. Mar Pet Geol 17, 285–342.
880   https://doi.org/10.1016/S0264-8172(99)00011-2

881   Sneh, A., 1988. Regional lithostratigraphy of the Eocene Avedat Group, Israel. Jerusalem.

882 Speijer, R.P., 1994. Paleocene sea-level fluctuations recorded in benthic foraminiferal
883   assemblages from gebel oweina (Esna, Egypt): Local, regional or global patterns? GFF
884   116, 63–65. https://doi.org/10.1080/11035899409546158

885 Sulpis, O., Agrawal, P., Wolthers, M., Munhoven, G., Walker, M., Middelburg, J.J., 2022.
886   Aragonite dissolution protects calcite at the seafloor. Nat Commun 13.
887   https://doi.org/10.1038/s41467-022-28711-z

888 Summons, R.E., Albrecht, P., McDonald, G., Moldowan, J.M., 2008. Molecular
889   biosignatures. Space Sci Rev 135. https://doi.org/10.1007/s11214-007-9256-5

890 Talling, P.J., Hage, S., Baker, M.L., Bianchi, T.S., Hilton, R.G., Maier, K.L., 2023. The
891   Global Turbidity Current Pump and Its Implications for Organic Carbon Cycling. Ann
892   Rev Mar Sci. https://doi.org/10.1146/annurev-marine-032223-103626

893 Tenzer, R., Gladkikh, V., 2014. Assessment of density variations of marine sediments with
894   ocean and sediment depths. The Scientific World Journal 2014.
895   https://doi.org/10.1155/2014/823296

896 Thomas, E., Zachos, J.C., Bralower, T.J., 2010. Deep-sea environments on a warm earth:
897   latest Paleocene-early Eocene, in: Warm Climates in Earth History.
898   https://doi.org/10.1017/cbo9780511564512.006

899 Wetzel, A., Uchman, A., 2018. The former presence of organic matter caused its later
900   absence: Burn-down of organic matter in oceanic red beds enhanced by bioturbation
901   (Eocene Variegated Shale, Carpathians). Sedimentology 65.
902   https://doi.org/10.1111/sed.12436

903 Wetzel, A., Uchman, A., 2001. Sequential colonization of muddy turbidites in the Eocene
904   Beloveža Formation, Carpathians, Poland. Palaeogeogr Palaeoclimatol Palaeoecol 168.
905   https://doi.org/10.1016/S0031-0182(00)00254-6

906 Woodcock, N.H., 1979. Sizes of submarine slides and their significance. J Struct Geol 1,
907   137–142. https://doi.org/10.1016/0191-8141(79)90050-6

908